Revealing hidden information with quadratic products of acoustic field amplitudes

David R. Dowling

Revealing Hidden Information With Quadratic Products of Acoustic Field Amplitudes

David R. Dowling

Department of Mechanical Engineering, University of Michigan, Ann Arbor MI 48109-2133

Abstract

Acoustic waves are omnipresent in modern life and are well described by the linearized equations of fluid dynamics. Once generated, linear acoustic waves carry and collect information about their source and the environment through which they propagate, and this information may be retrieved by analyzing recordings of these waves. Because of this, acoustics is the primary means for imaging and remote sensing in otherwise opaque environments, such as the Earth's oceans and crust, and the interior of the human body. For these information-retrieval tasks, acoustic fields are nearly always interrogated within their recorded frequency range or bandwidth. However, this frequency-range restriction is not general; acoustic fields may also carry hidden information at frequencies outside their bandwidth that can be revealed by analyzing the quadratic products of a pair of complex frequency-domain field amplitudes having different frequencies. The two unique quadratic field products, known as the frequency-difference and frequency-sum autoproducts, can be utilized for remote sensing at the difference and sum of the two constituent frequencies, respectively, even if these difference and sum frequencies lie outside the recorded field's bandwidth. Despite some fundamental limitations, forming and analyzing the autoproducts enables a variety of acoustic remote sensing applications that were long thought to be impossible. In particular, analysis of the frequency-difference autoproduct allows the detrimental effects of sparse-array recordings, random scattering, and other unknown source-to-receiver propagation effects to be suppressed when the recorded acoustic field has sufficient bandwidth. Examples and applications from laboratory and ocean propagation experiments are provided that involve frequencies from a few Hertz to more than 100 kHz, and propagation distances from tens of centimeters to more than 100 kilometers.

I. Introduction

Acoustics is the small fluctuation theory of fluid dynamics. Acoustic fields in unconfined environments take the form of traveling waves that carry and collect information about the source from which they were generated, and the environment though which they have propagated, respectively. Air- and water-borne acoustic waves permeate modern life as the primary means for human communication and ocean exploration, respectively. When extended beyond Newtonian fluids to soft and solid materials, acoustic waves are the preferred means for imaging within the human body, for non-destructively inspecting structures, for finding natural resources within Earth's crust, and for understanding and monitoring Earth's geophysical activity.

The classical equations of acoustics in a fluid are readily derived from the continuity equation, Euler's equation, and the thermodynamic relationship(s) for the fluid through simplification and linearization [1]. The resulting first-order partial-differential equations may be combined into a single inhomogeneous equation for the (real) time-domain acoustic pressure field, $p(\mathbf{r},t)$:

$$\nabla^2 p(\mathbf{r},t) - \frac{1}{c^2(\mathbf{r})}\frac{\partial^2}{\partial t^2}p(\mathbf{r},t) = -s(t)\delta(\mathbf{r}-\mathbf{r}_s)$$

(1)

Here, $\mathbf{r}$ is the three dimensional coordinate, t is time, $c(\mathbf{r}) \equiv [(\partial p/\partial \rho)_s]^{1/2}$ is the speed of sound, ρ is the fluid density, the undisturbed fluid is presumed to be compressible and stationary with uniform density, and the acoustic source is assumed to be compact and omni-directional. Although dipole, quadrupole, and extended fluid-dynamical acoustic sources are possible, this omni-directional point-source assumption is common in acoustic remote sensing. Interestingly, (1) also applies to compression waves in isotropic solids when $c(\mathbf{r})$ is obtained from the appropriate equation of state [2].

Because (1) is a linear equation, its solutions, $p(\mathbf{r},t)$, are often analyzed as a continuous superposition of sinusoidal disturbances with varying temporal frequency ω. Applying a Fourier transform to (1) moves acoustic analysis to the frequency domain where the governing equation is the inhomogeneous Helmholtz equation:

$$\nabla^2 P(\mathbf{r},\omega) + \frac{\omega^2}{c^2(\mathbf{r})}P(\mathbf{r},\omega) = -S(\omega)\delta(\mathbf{r}-\mathbf{r}_s)$$

(2)

Here, $P(\mathbf{r},\omega)$, the Fourier transform of $p(\mathbf{r},t)$, is a complex-valued function that depends on location and frequency and is commonly referred to as the complex field or complex amplitude, and $S(\omega)$ is the Fourier transform of the source waveform $s(t)$. The Helmholtz equation is a linear equation, so a sum of a particular solution and one or more homogeneous solutions is also a solution. However, a *product* of Helmholtz equation solutions at two different in-band frequencies may unexpectedly mimic or retain some or all of the characteristics of a Helmholtz equation solution at the difference or sum frequencies. This solution-product property is exact for plane waves in a uniform environment, and it can persist – with some limitations – for more general wave fields, too [3]. Its mathematical origins, experimental validation, and its novel utilization for unique acoustic remote sensing results are the primary topics of this article. For simplicity, only quadratic wave-field products are considered here. Extensions to cubic, quartic, and higher-order field products are clearly possible, but are beyond the scope of this article.

Analytical or numerical Fourier transforms are routinely employed to switch between the time domain, the realm of acoustic measurements, and the frequency domain, the preferred realm of acoustic analysis. Thus, results for both $p(\mathbf{r},t)$ and $P(\mathbf{r},\omega)$ are presented here, with the former appearing as experimental recordings and the latter occupying a pivotal place in mathematical definitions, developments, and comparisons. In the frequency domain, the frequency range through which an acoustic field has non-negligible amplitude is known as the field's bandwidth. Here, again for simplicity, acoustic fields are presumed to have a single well-defined bandwidth of nonzero extent: $\Omega_L \leq \omega \leq \Omega_H$, where Ω_L and Ω_H are the low- and high-frequency limits. The frequencies within and outside of this bandwidth are referred to as *in-band* and *out-of-band* frequencies, respectively, with the out-of-band frequencies further divided into *below-band* and *above-band* frequency ranges (see Fig. 1).

Remote sensing is the act of fully or partially recovering source and environmental information embedded in an acoustic field by analyzing field recordings made at one or more locations. Across the various fields and applications of acoustic remote sensing, the range of

possible signal frequencies spans 10 orders of magnitude, but many important applications are currently only possible within a fixed range of frequencies because acoustic source, acoustic propagation, or environmental characteristics beyond that frequency range are unfavorable. Thus, after nearly a century of development, existing signal processing techniques in acoustics (and beyond) confine remote sensing to in-band frequencies. However, such confinement is not a general limitation. Acoustic fields are shown herein to be richer with information so that the possibilities for acoustic remote sensing are actually more extensive. The purpose of this article is to demonstrate the validity of these contentions about acoustic fields and their utilization for remote sensing. In particular, it is shown herein that non-zero-bandwidth acoustic fields carry hidden out-of-band information that can be revealed though analysis of quadratic (or higher) products formed from $P(\mathbf{r},\omega)$ [3,4], and that this hidden information can be leveraged to produce successful remote source localization results that are not possible with conventional means [5-9].

The procedure for revealing the information hidden in acoustic fields is inspired by the nonlinear triad interactions that occur in turbulent flow [10,11]. The nonlinearity inherent in the Navier-Stokes equations can combine two spatial Fourier wave components with different wave numbers $\mathbf{k}_\pm$ ($|\mathbf{k}_+| > |\mathbf{k}_-|$) to *cascade* to higher wave number components when the original wave numbers are at least partially aligned ($|\mathbf{k}_+ + \mathbf{k}_-| > |\mathbf{k}_\pm|$), or to *backscatter* to lower wave number components when the original wave numbers are at least partially anti-aligned ($|\mathbf{k}_+ + \mathbf{k}_-| < |\mathbf{k}_\pm|$). In an acoustic field, the dispersion relationship derived from (1), $|\mathbf{k}|^2 = \omega^2/c^2$, links each (spatial) wave number with a (temporal) frequency. Thus, at each point in space, an intentionally formed quadratic product of complex amplitudes, $P(\mathbf{r},\omega_\pm)$, from the same location in the acoustic field but at two different frequencies, $\omega_\pm = \omega \pm \Delta\omega/2$, should generate higher- and lower-frequency field components, in a manner akin to heterodyning, when the two fields' wave numbers are aligned and anti-aligned, respectively. Interestingly, such alignment or anti-alignment is possible between the wave components that comprise an acoustic field by forming the field product without or with complex conjugation of the lower-frequency field. Such intentionally-formed acoustic-field products, referred to herein as *autoproducts*, have been found to contain out-of-band information hidden in the in-band acoustic field. However, the autoproducts also contain undesired quadratic-product artifacts that must be accounted for or suppressed in order to reveal their out-of-band information.

The remainder of this article is divided into four sections. Section II provides the mathematical basis and formulation for how out-of-band field information can be revealed from in-band field recordings. Section III illustrates the procedure using theoretical and experimental results for a simple half-space environment (aka Lloyd's mirror). Section IV provides comparisons of conventional in-band and unique below-band remote unknown-source localization results in three imperfectly known environments: a laboratory water tank with strong random scattering, and shallow and deep ocean waveguides having unknown sound-speed and boundary fluctuations. In each case, the acoustic field is recorded with a linear array of transducers and the remote localization is attempted in the plane defined by the source and the array. In all three cases, the conventional (in-band) approach fails to localize the source, while the below-band results, which sacrifice resolution in favor of robustness, are successful. Section V summarizes the research reported here, and provides the conclusions drawn from it.

II. Formulation

The starting point for revealing an acoustic field's hidden out-of-band information is the construction of the two unique quadratic products of the linear complex acoustic field, $P(\mathbf{r},\omega)$, at

two different frequencies, ω_+ and ω_-. These two field products are referred to herein as the frequency-difference (AP_Δ) and frequency-sum (AP_Σ) autoproducts, and are defined by:

$$AP_\Delta(\mathbf{r},\omega,\Delta\omega) \equiv P(\mathbf{r},\omega_+)P^*(\mathbf{r},\omega_-), \text{ and } AP_\Sigma(\mathbf{r},\omega,\Delta\omega) \equiv P(\mathbf{r},\omega_+)P(\mathbf{r},\omega_-). \tag{3a,b}$$

Here, the asterisk denotes a complex conjugate, $\Delta\omega = \omega_+ - \omega_-$ is the difference frequency, and $\Sigma\omega = \omega_+ + \omega_- = 2\omega$ is the sum frequency. The frequency-difference and -sum autoproducts may be notionally associated with the turbulent *backscatter* and *cascade* processes mentioned in the penultimate paragraph of Section I. The two autoproducts satisfy inhomogenous Helmholtz equations at the difference and sum frequencies, respectively [3], with a modified source term at the true source location and, when the in-band field is composed of multiple waves, an additional distributed-source term.

Both source terms generate artifacts in the autoproduct fields. The artifacts from the modified source term must be accounted for in acoustic remote sensing, and are typically important near and down-range from large in-band field amplitude gradients. The artifacts in the autoproduct fields from the distributed source term can be partially or fully suppressed by bandwidth averaging [3,4]. Appropriate bandwidth averages, denoted by angle brackets, are given by:

$$\langle AP_\Delta \rangle(\mathbf{r},\Delta\omega) = \frac{1}{\Omega_\Delta} \int_{\Omega_c - \frac{\Omega_\Delta}{2}}^{\Omega_c + \frac{\Omega_\Delta}{2}} \frac{AP_\Delta(\mathbf{r},\omega,\Delta\omega)}{S(\omega_+)S^*(\omega_-)} d\omega, \ \langle AP_\Sigma \rangle(\mathbf{r},\Sigma\omega) = \frac{1}{\Omega_\Sigma} \int_0^{\Omega_\Sigma} \frac{AP_\Sigma(\mathbf{r},\omega,\Delta\omega)}{S(\omega_+)S(\omega_-)} d(\Delta\omega),$$

$$\tag{4a,b}$$

where $\Omega_C = (\Omega_L + \Omega_H)/2$ defines the in-band center frequency, and $\Omega_\Delta = \Omega_H - \Omega_L - \Delta\omega$ and $\Omega_\Sigma = \min(2\Omega_H - \Sigma\omega, \Sigma\omega - 2\Omega_L)$ define the signal bandwidths available for averaging AP_Δ and AP_Σ, respectively. Note that Ω_Δ and Ω_Σ take on the maximum value of $\Omega_H - \Omega_L$ at $\Delta\omega = 0$ and $\Sigma\omega = 2\Omega_C$, respectively. Here, even though the full difference- and sum-frequency bandwidths ($0 \leq \Delta\omega \leq \Omega_H - \Omega_L$ and $2\Omega_L < \Sigma\omega < 2\Omega_H$, respectively) may include some in-band frequencies, $\Delta\omega$ and $\Sigma\omega$ are still termed *out-of-band* for convenience.

As defined above in (3), the autoproducts are simple quadratic field products. However, when integrated, as in (4), they share features with other better-known concepts and topics. In particular, when (3a) and (4a) are collected together, the integration over ω causes $<AP_\Delta>$ to become a signal-spectrum-normalized frequency-domain autocorrelation function. However, when (3b) and (4b) are collected together, the integration over $\Delta\omega$ causes $<AP_\Sigma>$ to be an entirely different type of integrated spectral product. In addition, the frequency-difference autoproduct is also related by single Fourier transforms to the Wigner-Ville transform and the ambiguity function from the field of bilinear time-frequency analysis [12,13]. The shifting to lower and higher frequencies is also an attribute of the parametric array [14]; however, the out-of-band frequencies generated by the parametric array exist due to hydrodynamic and thermodynamic nonlinearities induced by high-amplitude waves from a local oscillator, whereas autoproducts are created through an intentional multiplication of linear-field complex amplitudes after the field is recorded. A quadratic product of complex field amplitudes at a pair of frequencies is reminiscent of the mutual coherence function in statistical optics [15,16], and the formative concepts for Δk-radar [17-19]. However, unlike these related concepts and techniques, autoproducts do not

require ensemble averaging, and phase information is retained in the final quantities of interest. Overall, the autoproducts defined in (3) differ from these better-known concepts and topics in that they do not require an ensemble of complex field samples, additional Fourier transforms, high amplitude sound, a local frequency reference, or specialized signal broadcasts.

The bandwidth-averaged autoproducts may mimic genuine acoustic fields at the chosen difference ($\Delta\omega$) or sum ($\Sigma\omega$) frequency and their capacity for such field mimicry is illustrated in Section III. They are defined in (4) for this illustration purpose only, and are not used for the source localization results presented in Section IV because they involve the source signal spectrum, $S(\omega)$, which is unknown for a remote unknown source. However, the source-signal-spectrum normalizations in (4) cause the frequency-averaged autoproducts to mimic the Green's-function solutions of (2) when $S(\omega) = 1$ at the difference and sum frequencies, $G_\Delta(\mathbf{r})$ and $G_\Sigma(\mathbf{r})$, respectively. And, for the illustrations provided in Section III, these Green's functions are readily obtained from Lord Rayleigh's method of images using an appropriately modified boundary condition. Boundary condition modifications may be necessary when matching true fields to autoproducts because the quadratic products cause the reflection coefficient felt by an autoproduct field to differ from that felt by the in-band acoustic field from which they are obtained [3,4]. And, as a final point, the field mimicry possible with the frequency-averaged autoproducts cannot be extended to predict the characteristics of acoustic fields co-existing in the same environment at different frequencies because the response of a linear time-invariant system (the acoustic environment) in separate, non-overlapping frequency bands can be totally unrelated. Alternatively stated in musical terms, the relatively high-frequency sound from a flute cannot be used to mimic the lower-frequency sound produced by a trombone when both instruments are played at the same time in the same concert hall but at different locations on the stage. However, the frequency-difference autoproduct would allow the flute's sound to be processed in the trombone's musical register to localize the flute.

In the next section, direct comparisons of autoproducts and out-of-band fields are shown. To facilitate these comparisons, a normalization must be performed since autoproducts and ordinary acoustic fields have different units (pressure-squared vs. pressure). The normalization used here is

$$\left(\cdots\right)^{norm} = \left(\cdots\right)\left[\frac{1}{V}\int_V \left|\left(\cdots\right)\right|^2 dV\right]^{-1/2}$$

(5)

where $\left(\cdots\right)^{norm}$ denotes the normalized version of the field quantity $\left(\cdots\right)$, and V is the spatial region of interest. After normalization, the figure of merit considered here for how closely two fields align is the spatial cross-correlation coefficient, χ, defined by

$$\chi_{\Delta,\Sigma} \equiv \mathrm{Re}\left\{\frac{1}{V}\int_V \left(\left\langle AP_{\Delta,\Sigma}\right\rangle(\mathbf{r})\right)^{norm}\left(G_{\Delta,\Sigma}^*(\mathbf{r})\right)^{norm} dV\right\},$$

(6)

where the 'Δ' and 'Σ' subscripts denote quantities associated with the frequency-difference and frequency-sum autoproducts, respectively, and the frequency argument of the bandwidth-averaged autoproducts has been dropped for clarity and conciseness. The cross-correlation coefficient χ is constrained, $-1 \leq \chi \leq +1$, with a perfect match of normalized fields within V

corresponding to $\chi = 1$, and a perfect lack of correlation corresponding to $\chi = 0$. In addition, $2(1 - \chi)$ is the normalized mean-square difference between a bandwidth-averaged autoproduct and the out-of-band field it mimics.

III. Fields and Autoproducts in a Half-Space Environment

A direct test of the claim that the frequency-averaged autoproducts mimic out-of-band acoustic fields was undertaken in a simple half-space environment (Lloyd's mirror) where $P(\mathbf{r}, \omega)$ is well known from theory and is readily measured in a laboratory water tank, too [4]. A schematic of the experimental set up and the range-depth (r, z) coordinate system are shown in Fig. 2. The air-water interface ($z = 0$) provided a flat reflecting surface with a reflection coefficient of -1 for sound within the water. The broadcast transducer was located at depth $d = 200$ mm and emitted a 50-μs Gaussian-enveloped sinusoidal pulse with an in-band frequency range from $\Omega_L/2\pi = 40$ kHz to $\Omega_H/2\pi = 110$ kHz. This bandwidth included 99.9% of the signal energy. The field measurements reported here were made on a vertical line segment ($0 \leq z \leq 400$ mm) at a source-to-receiver horizontal distance of $r = 325$ mm. The receiver was moved with a vertical traverse in 1 mm steps for $0 \leq z \leq 100$ mm and in 5 mm steps for $100 \leq z \leq 400$ mm. The experimental recordings were collected at a rate of 2.0 mega-samples per second per channel. The recorded signals were time windowed to only include contributions from the direct and reflected paths. This meant zeroing out all data recorded more than 0.6 to 0.7 ms after the source broadcast. Standard numerical Fourier transform techniques were used to switch these windowed time-domain data to the frequency domain. At each receiver depth, the experiment was repeated three times for a total of 483 recordings. The signal spectrum $S(\omega)$ was determined from a coherent average of the measured direct-path pulse from all receiver depths where the direct- and reflected-path pulses were well-separated. In addition, small overall geometrical and sound-speed corrections were made within the known ranges of experimental uncertainties to increase the correlation of the measured and theoretical in-band fields.

The following analytical fields from this simple two-path environment were then compared to the measured field and its autoproducts. The theoretical in-band Green's function for the Lloyd's mirror environment is:

$$G(r, z, \omega) = \frac{P(r, z, \omega)}{S(\omega)} = \frac{e^{i\omega\tau_1}}{r_1} - \frac{e^{i\omega\tau_2}}{r_2}$$

(7)

where i is the imaginary root, $r_{2,1} = [r^2 + (z \pm d)^2]^{1/2}$ are the reflected and direct ray-path lengths, respectively, $\tau_{1,2} = r_{1,2}/c$ are the corresponding travel times, and the final term represents the reflected path. When (7) is inserted in (3) and (4), the following theoretical bandwidth-averaged autoproducts are found:

$$\langle AP_\Delta \rangle (r, z, \Delta\omega) = \frac{e^{i\Delta\omega\tau_1}}{r_1^2} + \frac{e^{i\Delta\omega\tau_2}}{r_2^2} - 2\frac{e^{i\Delta\omega(\tau_1+\tau_2)/2}}{r_1 r_2}\cos(\Omega_C\Delta\tau)\operatorname{sinc}\left(\frac{\Omega_\Delta\Delta\tau}{2}\right)$$

(8a)

$$\langle AP_\Sigma \rangle (r, z, \Sigma\omega) = \frac{e^{i\Sigma\omega\tau_1}}{r_1^2} + \frac{e^{i\Sigma\omega\tau_2}}{r_2^2} - 2\frac{e^{i\Sigma\omega(\tau_1+\tau_2)/2}}{r_1 r_2}\operatorname{sinc}\left(\frac{\Omega_\Sigma\Delta\tau}{2}\right)$$

(8b)

where $\Delta\tau = \tau_2 - \tau_1$ is the difference in travel times, and $\text{sinc}(x) = \sin(x)/x$. The first two terms in (8a) and (8b) arise from *same-path* products (direct-direct and reflected-reflected). The final term in (8a) and (8b) arises from *cross-path* products (direct-reflected and reflected-direct, simplified to a single term).

The same-path terms in (8) are similar, but not identical, to the field in (7) evaluated at $\Delta\omega$ or $\Sigma\omega$, thus, they can potentially correlate strongly with an out-of-band acoustic field when the additional (artifact) denominator factors of r_1 and r_2 in (8) do not vary significantly in the region of interest [3]. Additionally, the reflected-reflected terms in (8) both carry a positive sign, while the reflected-path term in (7) carries a negative sign. This sign difference arises because the quadratic products rectify the surface's -1 reflection coefficient. Consequently, the autoproduct fields in (8) appear to mimic genuine out-of-band acoustic fields in a Lloyd's mirror environment having a surface reflection coefficient of $+1$.

The cross-path terms in (8) are not present in (7). Thus, they permit or inhibit the autoproducts' potential mimicry of genuine fields, depending on their magnitude compared to the same-path terms. The cross-path terms' magnitudes are controlled by the sinc functions in (8), and should be relatively small when $\Omega_{\Delta,\Sigma}\Delta\tau \gg 2\pi$. However, when the receiver depth z is small, $\Delta\tau$ may approach zero. Thus, the autoproducts' mimicry of out-of-band fields may be reduced at shallow receiver depths.

Comparisons of the real parts of theoretical and measured normalized Green's functions are shown as functions of the measurement depth in the five panels of Fig. 3 at the signal's center frequency of $\Omega_C/2\pi = 75$ kHz (a), at below-band frequencies of $\Delta\omega/2\pi = 5$ kHz (b) and 30 kHz (c), and at above-band frequencies of $\Sigma\omega/2\pi = 150$ kHz (d) and 185 kHz (e). All five panels have the same horizontal (depth from 0 to 400 mm) and vertical (normalized amplitudes from -2.5 to $+2.5$) axis ranges, and all show the measurements as red 'x's. In Fig. 3a), the black curve is (7) evaluated using the minus sign shown. In Fig. 3b)-e), the black curves are the appropriate versions of (8), and the blue dotted curves are (7) evaluated with a plus sign between the two terms. The vertical dashed lines in Fig. 3b)-e) are located at the depth where $\Omega_{\Delta,\Sigma}\Delta\tau = 2\pi$ in each case; an autoproduct is not expected to mimic its counterpart out-of-band field to the left of these dashed lines.

All parts of Fig. 3 show excellent matching between the various fields, and this matching persists at frequencies and source-array ranges not shown here [4]. Figure 3a) illustrates the quality of the in-band matching, $\chi = 0.986$, found between (7) and the measurements. This correlation value is maintained within a few percent throughout the in-band frequency range (40 kHz to 110 kHz). The remaining panels of Fig. 3 illustrate the quality of the out-of-band matching found between the autoproducts and (7) with a plus sign between terms. Here, all possible cross correlations between autoproducts and theoretical fields are above 0.972, even when V is conservatively chosen to be the entire line segment from $z = 0$ to 400 mm. This minimum correlation rises to 0.987 when the shallow receiver depths to the left of the vertical lines in Fig. 3b)-e) are excluded. The remaining mismatch between the normalized autoproducts and out-of-band fields is attributed to quadratic-product and experimental artifacts. Overall, the results shown in Fig. 3 indicate that a measured acoustic field with a 40-to-110 kHz bandwidth can be used to produce field information at frequencies outside that range.

IV. Conventional and Frequency-Difference Source Localization

If the autoproducts' carry out-of-band acoustic-field information, then they should provide novel results and capabilities when interrogated using conventional remote sensing techniques. This section provides three such examples where the frequency-difference autoproduct is used for localization of a remote unknown source in an acoustic environment with unknown complications.

Although the source-to-receiver propagation scenario is nearly identical to that described in the prior section, the emphasis and information flow in a source-localization effort are different. Here the source's waveform and location are unknown, but the acoustic field is recorded simultaneously at multiple locations, $\mathbf{r}_j$, allowing AP_Δ to be constructed at these locations, too. Although there are many acoustic-source localization schemes [20], the most common and versatile frequency-domain approaches – plane-wave beamforming, spherical-wave beamforming, and matched field processing (MFP) – involve spatially correlating the measured P-field with a computed field (w) at the same frequency [21]. For MFP, the computed field is typically a Green's function with a hypothesized source location, $\mathbf{r}_t$, that is scanned throughout the region of interest in search of the location(s) where the measured and computed fields show high correlation. These high-correlation locations are presumed to be possible source locations. For the present purposes, the process is generically described by:

$$B(\mathbf{r}_t) = \left\langle \left| \sum_{j=1}^{N} \left(P(\mathbf{r}_j, \omega) \right)^{norm} \left(w^*(\mathbf{r}_j, \mathbf{r}_t, \omega) \right)^{norm} \right|^2 \right\rangle,$$

(9)

where $B(\mathbf{r}_t)$ is the normalized in-band cross-correlation magnitude-squared and, when plotted, is known as an ambiguity surface when $\mathbf{r}_t$ (the search coordinate) involves two or more spatial coordinates; N is the number of locations where the complex field $P(\mathbf{r}_j, \omega)$ is known; $w(\mathbf{r}_j, \mathbf{r}_t, \omega)$ is the computed field; the angle brackets indicate an average through the in-band frequency range; and the normalization of P and w ensure $0 \leq B(\mathbf{r}_t) \leq 1$. B can be interpreted as the likelihood that $\mathbf{r}_t$ is a true source location, and is commonly reported in decibels (dB) as $10\log_{10}[B(\mathbf{r}_t)]$. To evaluate (9), the w-field computations may involve the well-known algebraic forms for plane or spherical waves, or multi-dimensional numerical propagation simulations that include reflection, refraction, diffraction, and multipath propagation [21]. In ideal circumstances, the resolution and performance provided by source localization schemes based on (9) improve when ω and N increase. Unfortunately, ideal circumstances are seldom realized in practice and source localization schemes based on (9) often fail because: simple w-fields may not match the measured P-fields when: the acoustic propagation is complicated; sophisticated propagation computations of w require extensive and accurate environmental information that may not be available; and the number and spacing of field measurement locations may be too few or too large, respectively.

When the maxima of $B(\mathbf{r}_t)$ indicate true source locations, the approach described by (9) is considered successful. However, mismatch between P and w arising from wave-front differences and/or imperfect environmental knowledge may prevent localization success. In general, mismatch problems increase with increasing frequency and source-receiver range. For example, prior water-tank experiments suggest that acoustic ray-path lengths must be known to better than one third of an acoustic wavelength for beneficial field matching [22]. In the ocean, where wavelengths from fractions of a meter to tens of meters and source-receiver ranges from several to several hundred kilometers are of interest, the requisite environmental knowledge is not

8

generally available. In addition, when the acoustic wavelength is small compared to the source-receiver distance in a complicated environment, the necessary *w*-field computations may be excessively time consuming.

The frequency-difference autoproduct provides a potential remedy for the field-mismatch and field-computation-time problems since it can provide below-band wave-field information at frequencies where mismatch and computations are less problematic. To implement this remedy, two changes to (9) are needed. First, the measured field should be replaced by AP_Δ from (3); and second, the computed field should be evaluated at the below-band frequency $\Delta\omega$.

$$B_\Delta(\mathbf{r}_t, \Delta\omega) = \left\langle \left| \sum_{j=1}^N \left(AP_\Delta(\mathbf{r}_j, \Delta\omega) \right)^{norm} \left(w^*(\mathbf{r}_j, \mathbf{r}_t, \Delta\omega) \right)^{norm} \right|^2 \right\rangle.$$

(10)

Here, $\Delta\omega$ may be chosen within $0 \le \Delta\omega \le \Omega_H - \Omega_L$ to achieve the desired level of robustness to field mismatch and reduction in computational cost while maintaining a sufficient level of resolution. In short, the schemes embodied in (9) and (10) provide a user-adjustable trade-off between the in-band frequency range ($\Omega_L \le \omega \le \Omega_H$), where higher resolution is possible but field-mismatch and computational expense may be problematic, and the lower difference-frequency range, where resolution is lower but field-mismatch and computational expense are reduced as well.

The final analytical step (9) and (10) is a signal-bandwidth average that is undertaken to improve the robustness of the localization results by ensuring that $B(\mathbf{r}_t)$ and $B_\Delta(\mathbf{r}_t, \Delta\omega)$ are based on the entire recorded signal, and not just a single frequency or single pair of frequencies. However, it should be noted that (10) does not involve the signal-bandwidth-averaged autoproduct defined in (4a). Instead, the signal-bandwidth average in (10) occurs after AP_Δ and w^* have been multiplied together, the sum over array elements has been completed, and the magnitude-squared operation has been performed.

Direct comparisons between in-band source localization results from (9) and below-band localization results from (10) are provided in the following three subsections for: (A) a laboratory water-tank experiment that included strong random scattering, (B) a shallow ocean experiment that included random scattering from internal waves and multipath propagation caused by reflecting surfaces [6,8], and (C) a deep ocean experiment that included random scattering from internal waves and multipath propagation caused by reflecting surfaces and refraction. In all three cases, the experiments were conducted in water where the nominal sound speed is $c = 1500$ m/s; the signal was broadcast by a single source and recorded with a linear receiving array; and remote source localization was attempted in the plane defined by the source and the array. Measured and computed time-domain waveforms or wave-fronts, corresponding to $P(\mathbf{r}_j, \omega)$ and $w(\mathbf{r}_j, \mathbf{r}_t, \omega)$, are shown along with localization results from (9) and (10).

A. Laboratory Water Tank

These experiments were conducted in a quiescent cylindrical water tank (1.07 m diameter and 0.90 m water depth) with a nominally omni-directional source, 12 receiving hydrophones, and 18 scatterers (air-filled ping-pong balls) all located at mid-water-column. Figure 4 shows a picture of the setup looking through the water surface. The source is the black sphere at the end of the bronze pole in the left half of the picture. It was positioned 40 cm from the receiving array and 10 cm to the left of the array's center. If either localization scheme is successful, this

location should be highlighted by the extreme value of B and/or B_Δ. The receivers appear in a diagonal row near the top of the picture with the first (last) receiver positioned closest to the picture's left (right) edge. The distributed white spheres are the scatterers. Their placement and properties are considered unknown when computing $w(\mathbf{r}_j,\mathbf{r}_t,\omega)$ for use in (9) and (10). The source signal was a 250-μs Gaussian-windowed pulse with an in-band frequency range from 150 kHz to 200 kHz. The signal recordings were time windowed before processing to exclude reflections from the water surface and tank walls.

When taken together, the array geometry, the unknown scatterers, and the in-band frequency range create a challenging in-band localization scenario. At the center frequency of the signal pulse, the spacing between receivers is 6.0 wavelengths. This is substantially larger than the ideal Nyquist spacing of one half wavelength, making this a *sparse* receiving array that is likely to produce strong side-lobe ambiguities in its correlation output. Additionally, the scatterers are *strong* because of their large relative diameter (4.7 center-frequency wavelengths) and the great acoustic contrast between air and water. Thus, they are expected to significantly alter the recorded P-fields compared to the computed w-fields.

Measured and computed time-domain signals for this experiment are shown in Fig. 5a) and b), respectively. The vertical axis on both plots combines recorded signal values and receiver numbers, from 1 (the top time trace) to 12 (the lowest time trace). The recorded amplitude and pulse-envelope variations seen in the measured signals are the result of scattering and shadowing from the 18 scatterers. The computed signals are based on ideal free-space propagation and do not include the scatterers, but are provided for comparison to illustrate the extent of the field-mismatch in these experiments. The localization scheme embodied in (9) amounts to correlating the measured signals shown in Fig. 5a) with ideal signals – like those shown in Fig. 5b) – that originate from different source locations.

Figure 6 shows the source localization outputs, $B(\mathbf{r}_t)$ and $B_\Delta(\mathbf{r}_t,\Delta\omega)$, using the array recordings shown in Fig. 5a) for $\mathbf{r}_t = (x,y)$ lying in the horizontal plane defined by the source and the array. In both parts of Fig. 6, the array is located along the y-axis between y = ±28 cm; the white circle outlined in black indicates the true location of the source; the white triangle outlined in black indicates the location of the maximum value of either B within the 1-m-by-1-m search window; and B-values are provided with a dynamic range of 10 dB. The localization result shown in Fig. 6a) for the in-band scheme (9) is not successful. The actual and acoustically-determined locations are far apart and many maxima of B occur within the search window. However, the localization result shown in Fig. 6b) for the below-band scheme (10) evaluated at $\Delta\omega/2\pi$ = 20 kHz is successful. There is one dominant maximum of B_Δ and it is located within 1 cm of the true source location.

The trade-off between resolution and suppression of the mismatch is well illustrated here. The acoustic features in Fig. 6a) are narrower than those in Fig. 6b), but the field-mismatch introduced by the scatterers dominates the in-band result. Nevertheless, the out-of-band autoproduct-based result (using the same recordings) overcomes the field mismatch because the scatterers are weaker at the below-band frequency (20 kHz) where their diameter is approximately half a signal center-frequency wavelength.

B. Shallow Ocean

The experiments for this subsection were conducted in a 106-m-deep, downward-refracting, shallow-ocean waveguide off the coast of Kauai in 2011 [23]. Sound was broadcast 3 km along an isobath from sources at different depths to a 16-element vertical receiving array

10

deployed in the lower two-thirds of the water column. The source signal utilized here was a 100-ms-duration frequency sweep from 11.2 kHz to 32.8 kHz. The nominal experimental geometry is shown in Fig. 7 along with smoothed schematic renderings of the ocean's sound speed profile in shallow and deep water. However, the simplicity of the Fig. 7 drawing is misleading; the actual ocean-propagation environment was imbued with unknown complications arising from its dynamic rough surface, water-column depth and seabed composition variations, and depth-dependent sound-speed profile that varied in time because of oceanic internal wave heaving motions. Moreover, at the signal center frequency (22 kHz), the nominal acoustic wavelength (λ_C) is just 7 cm; thus, the path-length uncertainty (Δx) requirement for beneficial correlation contributions ($\Delta x < \lambda_C/3$) is unlikely to be met over the $R = 3$ km source-to-array range. All these complications increase the level of field mismatch, and when taken together, they prevent in-band source localization based on (9) from being successful. However, the below-band approach of (10) has shown some success [6,8].

Sample measured and computed (ideal) matched-filter time-domain signals for this experiment with a source depth of $Z = 60.2$ m are shown in Fig. 8a) and b), respectively. The plots show the arrival pattern of in-band acoustic wave fronts. The vertical axis of both plots combines recorded signal values and receiver depths, from the shallowest receiver (the top time trace) to the deepest receiver (the lowest time trace). The environmental information used to generate Fig. 8b) included the water column depth and a sound speed profile similar to that shown in Fig. 7 with a 5.2 m/s difference between $z = 0$ and 106 m. Although both parts of Fig. 8 show multiple wave-front arrivals at every depth, the arrival patterns are far from identical. In particular, the recordings in Fig. 8a) show a strong deep arrival between 8.5 and 10 ms and many weak scattered arrivals throughout the plotted time window; all are absent in Fig. 8b). In addition, the recorded signal amplitudes in the lower half of the water column are generally larger than those shown in the computed field.

Figure 9 shows the source localization outputs, $B(\mathbf{r}_t)$ and $B_\Delta(\mathbf{r}_t, \Delta\omega)$, using the array recordings shown in Fig. 8a) for $\mathbf{r}_t =$ (range, depth) in the vertical plane defined by the source and the array. In both parts of Fig. 9, the array is located along the vertical axis at zero range between $z = 41.2$ m and 97.4 m; the white circle outlined in black indicates the true location of the source; and B-values are provided with a dynamic range of 5 dB but with different absolute levels. The localization result shown in Fig. 9a) for the in-band scheme (9) is not successful. The B-values are low, and, at best, one might only be confident that the source was in the lower half of the water column since there are many maxima of B within the search window. However, the localization result shown in Fig. 9b) for the below-band scheme (10), averaged from $\Delta\omega/2\pi = 50$ Hz to 500 Hz and corrected to suppress cross-path product artifacts, is much more successful. There is a dominant maximum of B_Δ located within 90 m of the true source range and within 5.1 m of the true source depth. The 3-km-period correlation pattern seen in Fig. 9b) is an unavoidable artifact of this experiment's environment, and also occurs in source-localization simulations when field-mismatch is entirely absent. More complete analysis of this experimental data set suggests the below-band localization scheme can be successful in this environment up to the noted periodic limitation [6,8].

C. Deep Ocean

The experiments for this subsection were conducted in the Philippine Sea in 2010 [24] and involved a variety of sources at ranges up to several hundred kilometers broadcasting to a nearly water-column-spanning vertical array with 149 receivers. The source signal was a 135 s

frequency sweep from 200 to 300 Hz, and it was broadcast every 3 hours every other day for multiple months to collect an ensemble of hundreds of pulse recordings. The nominal experimental geometry is again shown in Fig. 7, but here the source depth is $Z = 1066$ m, the source-to-array range is $R = 129.4$ km, the water column depth is $D = 6$ km, and the deep-water sound speed profile is appropriate. For these experiments, the difference between the ocean surface and minimum sound speeds was approximately 50 m/s; thus, there was considerable refraction along with ocean-surface and seabed reflections that lead to complicated multipath sound propagation between the source and the array. And, as in the shallow ocean, unknown spatial fluctuations in the sound speed profile, oceanic surface and internal waves, and unknown ocean-floor depth and composition variations caused considerable field mismatch. Furthermore, at the signal center frequency (250 Hz), the acoustic wavelength is $\lambda_C \approx 6$ m; thus, the path-length uncertainty (Δx) requirement for beneficial correlation contributions ($\Delta x < \lambda_C/3$) is again unlikely to be met over the $R \approx 130$ km source-to-array range.

Sample measured and computed (ideal) matched-filter time-domain signals for this experiment are shown in Fig. 10a) and b), respectively. The vertical axis of both plots is depth (increasing downwards) from the ocean surface at $z = 0$ to the deepest receiver at $z = 5.3$ km, and the horizontal axis of both plots is the acoustic travel time, 86.4 s $\leq t \leq$ 88.4 s. The red stripe at the top of Fig. 10a) is noise from an experimental artifact. The environmental information used to generate Fig. 8b) included the water column depth and a sound speed profile, similar to that shown in Fig. 7 but measured near the vertical array.

Both parts of Fig. 10 show a complicated arrival pattern of weaker boundary-interacting arrivals that span all depths, and stronger refracted arrivals that form sharply-pointed overlapping 'v's between depths of 0.5 and 4 km. Although there are many similarities between the measured and computed arrival patterns, there are a number of differences, too, but not all contribute to field mismatch. First, there is an overall 0.3 to 0.4 s time shift between the arrival patterns in the two figures, but this shift does not contribute to the field mismatch problem. Second, the boundary-interacting arrivals are delayed compared to the refracted arrivals in the computation when compared to the measurements, especially in the lower half of the water column. This difference does contribute to the field mismatch problem. Third, the computed wave-front amplitudes and arrival times are smoothly varying while the measured ones are not, especially those of the boundary interacting arrivals. These variations also contribute to the field mismatch problem.

For this acoustic propagation scenario – as for the previous two – the in-band scheme fails while the out-of-band scheme is successful. After choosing a 300-km-by-6-km search plane and defining 'success' as the peak of B or B_Δ falling within 5% of the overall search range and depth (± 15 km in range and ± 300 m in depth) of the true source location, the in-band scheme produced only one successful localization when applied individually to the first 100 (correctly recorded) experimental pulses. Such dismal localization performance for this frequency range and source-to-receiving-array distance is expected and has led to the abandonment of in-band MFP localization schemes, outside of the research community, for such frequencies and distances. However, the below-band technique produced 85 successes when the outcome from (10) for individual pulses was averaged through three difference frequencies, $\Delta\omega/2\pi = 3.75$, 4.00 and 4.25 Hz; and a phase correction was applied to w to account for caustics along the 130 km propagation path. When the localization results from neighboring pulse pairs were ensemble averaged, these localization performance results remained at one success for the in-band scheme

but improved to 92 successes for the below-band scheme. Here, the one- and two-pulse in-band successes were from different pulse broadcasts, so they were likely obtained by random chance.

Scatter plots for the two-pulse-averaged results in the 300-km-by-6-km search plane are shown on Figure 11 for the in-band (a) and out-of-band (b) schemes. In both parts of Fig. 11, the blue squares mark the locations of the peaks of B or B_Δ, and the red ellipse defines the 'success' boundary. The inset panel in Fig. 11b) shows the cloud of successful out-of-band localization results. Additional difference-frequency and multiple-pulse ensemble averaging further improves the out-of-band results, too. Thus, in this scenario as well, the frequency-difference scheme (10) allows source localization when the equivalent in-band approach (9) fails.

V. Summary and Conclusions

Acoustic waves in fluid media are well described by the linearized equations of fluid motion. They provide a unique means for mankind to explore the interior of the Earth, its oceans, and the human body. Because of this, acoustic remote sensing is economically important and common place in the modern world. In the many applications of acoustic remote sensing that have been developed over many decades, recorded acoustic signals are analyzed within their (in-band) frequency range. However, this limitation to in-band analysis and information extraction is not a scientific one. This paper describes how a quadratic product of complex linear-field amplitudes can be used to reveal hidden information that lies outside of the frequency range of a recorded acoustic field. The results presented here show that this out-of-band information can be used to reconstruct above- and below-band acoustic fields when the original signal is known, or to achieve unique source localization results when the original signal is unknown. The reported work draws on experiments conducted in a laboratory water tank and in the ocean.

The following four conclusions are drawn from this effort. First, acoustic fields are unexpectedly richer in information than is typically thought. The results provided here suggest that an acoustic field with in-band frequency range $\Omega_L \leq \omega \leq \Omega_H$ also carries hidden information at lower frequencies, $0 < \Delta\omega < \Omega_H - \Omega_L$, and at higher frequencies, $2\Omega_L \leq \Sigma\omega \leq 2\Omega_H$. Second, this hidden acoustic information may be revealed by quadratic products of complex field amplitudes that down- and up-shift the spatial wave numbers of field components in a manner similar to the backscatter and cascade processes found within hydrodynamic turbulence. However, unlike naturally occurring fluid dynamic nonlinearities, the quadratic products considered here are formed after field recording and their formation may be controlled by the investigator to selectively reveal below-band or above-band hidden information at the frequency(ies) of interest. For example, the 6 and 30 kHz results shown in Fig. 3 are readily extended to any frequency below 60 kHz or so [4]. Third, the two possible quadratic products (the autoproducts) formed from complex acoustic field amplitudes at two different frequencies can be considered pseudo or surrogate fields that contain information at the difference or sum frequency of the two constituent field amplitudes, even when these frequencies lie outside the bandwidth of the original field. As shown herein, autoproduct fields contain out-of-band field information, and artifacts from their associated quadratic product that can be at least partially suppressed by averaging through the in-band frequency range. And fourth, use of these quadratic acoustic products in established remote sensing schemes can lead to unique results that surpass what is possible from direct use of the in-band field in the same schemes. The three sets of experimental results from three different environments in three-different (but overlapping) frequency ranges, support this conclusion. In addition, when the wave speed c is non-dispersive

[a necessary requirement in going from (1) to (2)], these four conclusions may apply to electromagnetic, seismic, and structural acoustic waves as well.

V. Acknowledgements

VI. References

[1] Pierce, A.D. (1989) *Acoustics*, Acoust. Soc. Am. through the Am. Inst. of Phys., Woodbury, New York, pp. 6-20.

[2] Fung, Y.C. (1965) *Foundations of Solid Mechanics*, Prentice-Hall, Inc., Edgewood Cliffs, New Jersey, pp. 186-187.

[3] Worthmann, B.M. and Dowling, D.R. (2017) "The frequency-difference and frequency-sum acoustic-field autoproducts," *J. Acoust. Soc. Am.*, Vol. 141(6), 4579-4590. http://dx.doi.org/10.1121/1.4985440

[4] Lipa, J.E., Worthmann, B.M., and Dowling, D.R. (2018) "Measurement of autoproduct fields in a Lloyd's mirror environment," *J. Acoust. Soc. Am.*, Vol. 143(4), 2419-2427. https://doi.org/10.1121/1.5032200

[5] Abadi, S.H., Song, H.-C., and Dowling, D.R. (2012) "Broadband sparse-array blind deconvolution using frequency-difference beamforming," *J. Acoust. Soc. Am.*, Vol. 132(5), 3018-3029. http://dx.doi.org/10.1121/1.4756920

[6] Worthmann, B.M., Song, H.C., and Dowling, D.R. (2015) "High frequency source localization in a shallow ocean sound channel using frequency difference matched field processing," *J. Acoust. Soc. Am.*, Vol. 138(6), 3549-3562. http://dx.doi.org/10.1121/1.4936856

[7] Douglass, A.S., Song, H.C., and Dowling, D.R. (2017) "Performance comparisons of frequency-difference and conventional beamforming," *J. Acoust. Soc. Am.*, Vol. 142(3), 1663-1673. http://dx.doi.org/10.1121/1.5003787

[8] Worthmann, B.M., Song, H.C., and Dowling, D.R. (2017) "Adaptive frequency-difference matched field processing for high frequency source localization in a noisy shallow ocean," *J. Acoust. Soc. Am.*, Vol. 141(1), 543-556. http://dx.doi.org/10.1121/1.4973955

[9] Abadi, S.H., Haworth, K.J., Mercardo-Shekhar, K.P., and Dowling, D.R. (2018) "Frequency-sum beamforming for passive cavitation imaging," to appear in *J. Acoust. Soc. Am.*, Vol. 144. https://doi.org/10.1121/1.5045328

[10] Waleffe, F. (1992) "The nature of triad interactions in homogeneous turbulence" *Phys. Fluids A*, Vol. 4(2), 350-363. https://doi.org/10.1063/1.858309

[11] Pope, S.B. (2000) *Turbulent Flows*, Cambridge Univ. Press, Cambridge, United Kingdom, pp. 606-609.

[12] Cohen, L. (1989) "Time-frequency distributions-a review." *Proceedings of the IEEE* 77(7), 941-981. https://doi.org/10.1109/5.30749

[13] Borcea, L., Papanicolaou, G., and Tsogka, C. (2006) "Adaptive interferometric imaging in clutter and optimal illumination." *Inverse Problems*, Vol. 22(4), 1405. https://doi.org/10.1088/0266-5611/22/4/016

[14] Westervelt, P.J. (1963) "Parametric acoustic array," *J. Acoust. Soc. Am.*, Vol. 35, 535-537. http://dx.doi.org/10.1121/1.1918525

[15] Beran, M. J. and Parrent, G. B. (1964) *Theory of Partial Coherence*. Englewood Cliffs, NJ: Prentice-Hall, Inc., Ch. 3.

[16] Born, M., and Wolf, E. (1999) *Principles of optics: Electromagnetic theory of propagation, interference, and diffraction of light*, Chapter 10, 7th ed. Cambridge, UK: Cambridge University Press.

[17] Weissman, D. (1973) "Two frequency radar interferometry applied to the measurement of ocean wave height." *IEEE Transactions on Antennas and Propagation*, Vol. 21(5), 649-656. https://doi.org/10.1109/TAP.1973.1140593

[18] Popstefanija, I., McQueen, D. S., and McIntosh, R. E. (1993) "A stepped-frequency delta-K microwave radar for oceanographic studies," *IEEE transactions on geoscience and remote sensing*, Vol. 31(3), 681-691. https://doi.org/10.1109/36.225534

[19] Sarabandi, K., and Nashashibi, A. (1999) "Analysis and Applications of Backscattered Frequency Correlation Function," *IEEE Transactions on Geoscience and Remote Sensing*, Vol. 37(4), 1895-1906.

[20] Dowling, D.R., and Sabra, K.G. (2015) "Acoustic remote sensing," *Annual Review of Fluid Mechanics*, Vol. 47, 221-243.

[21] Jensen, F.B., Kuperman, W.A., Porter, M.B., and Schmidt, H. (2011) *Computational Ocean Acoustics, 2nd ed*. Springer, New York.

[22] Williamson, L., Haapaniemi, E., and Dowling, D.R. (2014) "Sonar performance improvements using first reflections in matched-field processing" *Naval Engineers Journal*, Vol. 126, 103-107.

[23] Hodgkiss, W. S., Preisig, J. C. (2011). "Kauai Acomms MURI 2011 (KAM11) Experiment," *Proc. 11th European Conference on Underwater Acoustics (ECUA 2012)*, July 2 – 6, 2012, pp. 993-1000.

[24] Worcester, P.F., Dzieciuch, M.A., Mercer, J.A., Andrew, R.K., Dushaw, B.D., Baggeroer, A.B., Heaney, K.D., D'Spain, G.L., Colosi, J.A., Stephen, R.A., Kemp, J.N., Howe, B.M., Van Uffelen, L.J., and Wage, K.E. (2013) "The North Pacific Acoustic Laboratory deep-water acoustic propagation experiments in the Philippine Sea," *J. Acoust. Soc. Am.*, Vol. 134(4), 3359-3375. http://dx.doi.org/10.1121/1.4818887

Figure Captions

Figure 1. Time- and frequency domain representations of acoustic field waveforms. Acoustic recordings are made in the time domain (left) but are often transferred via a Fourier transform to the frequency domain (right) for analysis. The frequency range where the field has non-negligible complex amplitude is the field's bandwidth. *In-band* and *out-of-band* frequencies fall within and outside the field's bandwidth, respectively, with out-of-band frequencies occurring both below and above the field's in-band frequency range.

Figure 2. Schematic and coordinate system for a two-path laboratory water tank experiment intended to demonstrate that out-of-band field information is hidden within in-band signal recordings. A nominally omni-directional acoustic source located at $(r, z) = (0, d = 200$ mm) broadcasted a 40 kHz-to-110 kHz pulse. The receiver was placed at 161 locations on a vertical line segment from $z = 0$ (the water surface) to a depth of 400 mm at fixed horizontal distance of $r = 325$ mm.

Figure 3. Comparisons of measured and theoretical fields as a function of depth for the experimental setup shown in Fig. 2 (color on-line). In all panels, the amplitudes are normalized using (5) with V as the vertical line segment from depth = 0 to depth = 400 mm, and the measurements are shown with red '×'s. The measured field and theoretical in-band field (black curve) from (7) at 75 kHz are shown in a). The measured autoproducts are shown with theoretical autoproducts (black curves), and theoretical out-of-band fields from (7) with a plus sign between terms (blue-dotted curves) for below-band frequencies of $\Delta\omega/2\pi = 5$ kHz in b) and 30 kHz in c), and for above band frequencies of $\Sigma\omega/2\pi = 150$ kHz in d) and 185 kHz in e). The dashed vertical lines show the depth below which autoproducts should match out-of-band fields in the Fig. 2 environment. All five panels have the same horizontal axes and vertical axes, and show excellent matches between the various curves and measured data.

Figure 4. A picture looking through the water surface of the water-tank experimental setup. The source is the black sphere in the lower left quadrant of the picture at the end of the bronze pole. The receivers appear in a diagonal row near the top of the picture. The 18 distributed white spheres (air-filled ping-pong balls) are scatterers that complicate the source-to-array propagation and thereby hinder in-band source localization from the array-recorded signals alone.

Figure 5. Measured (a) and ideal (b) time-domain acoustic fields for the experimental setup shown in Fig. 4 for broadcast of a 200-μs Gaussian-windowed pulse with an in-band frequency

range from 150 kHz to 200 kHz. The measured field in (a) includes scattering while the ideal field in (b) does not.

Figure 6. Source localization correlation outputs from the recordings shown in Fig. 5a) (color on-line). The source location is marked by a white circle outlined in black. The correlation peak location is marked by a white triangle outlined in black. The receiving array is at x = 0 and |y| ≤ 28 cm. Panel a) shows in-band conventional results for $B(\mathbf{r}_t)$ from (9). Panel b) shows below-band frequency-difference results for $B_\Delta(\mathbf{r}_t,\Delta\omega)$ using (10) with $\Delta\omega/2\pi$ = 20 kHz. The below-band result is successful (the markers overlap) while the in-band technique is not.

Figure 7. Generic ocean experimental geometry showing a vertical array at $r = 0$, a sound source at range $r = R$ and depth $z = Z$, both in water of depth D. Sample depth-dependent sound speed profiles for the shallow and deep ocean experiments are shown at the right.

Figure 8. Measured (a) and computed (b) time-domain impulse responses obtained from matched filtering for the shallow-ocean experiment. The source signal utilized here was a 100-ms-duration frequency sweep from 11.2 kHz to 32.8 kHz. The measured impulse responses show more arrivals and the effects of scattering when compared to the computed ones.

Figure 9. Source localization correlation outputs from the recordings shown in Fig. 8a) (color on-line). The source location is marked by the white circle. The receiving array at $r = 0$ is shown by black dots. Panel a) provides in-band conventional results for $B(\mathbf{r}_t)$ from (9). Panel b) provides below-band frequency-difference results for $B_\Delta(\mathbf{r}_t,\Delta\omega)$ using (10) incoherently averaged from $\Delta\omega/2\pi$ = 50 Hz to 500 Hz. The in-band technique fails, but below-band result is modestly successful. The 3-km periodicity in b) is an unavoidable part of this acoustic environment.

Figure 10. Measured (a) and computed (b) time-domain impulse responses (aka time fronts) obtained from matched filtering for the deep-ocean experiment (color on-line). The source signal utilized here was a 135-s-duration frequency sweep from 200 Hz to 300 Hz. The orange stripe at the top of (b) is noise from an experimental artifact. The boundary interacting time fronts are the diagonal features that extend from the top to the bottom of both panels. The louder refraction-guided arrivals appear as zig-zags in the upper two thirds of each panel. The measured time fronts in (a) show less regularity and different timing than the computed time fronts in (b).

Figure 11. Two-pulse ensemble-averaged source localization scatter plots from the first 101 (correctly measured) experimental pulses from the deep-ocean experiment in a 300-km-range by 6-km-depth search plane (color on-line). Blue squares mark the locations of correlation maxima. The circle marks the location of the source. The red ellipse defines the localization-success boundary. Its dimensions are ±5% of the overall search range and depth. Panel a) shows in-band conventional results for $B(\mathbf{r}_t)$ from (9). Panel b) shows below-band frequency-difference results for $B_\Delta(\mathbf{r}_t,\Delta\omega)$ using (10) incoherently averaged across $\Delta\omega/2\pi$ = 3.75, 4.00 and 4.25 Hz with a phase correction applied to w to account for caustics along the 130 km propagation path. The in-band scheme is successful 1 time out of a 100. The below-band scheme is successful 92 times out of 100. In b), the inset plot shows the cloud of successful below-band localizations.
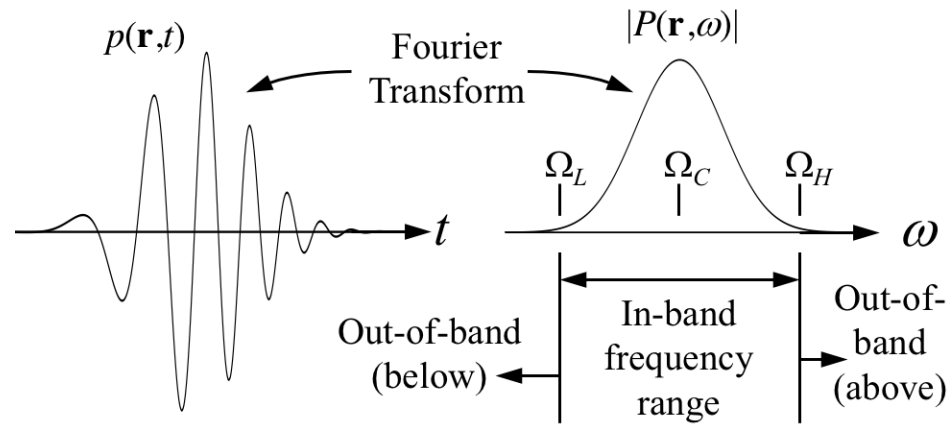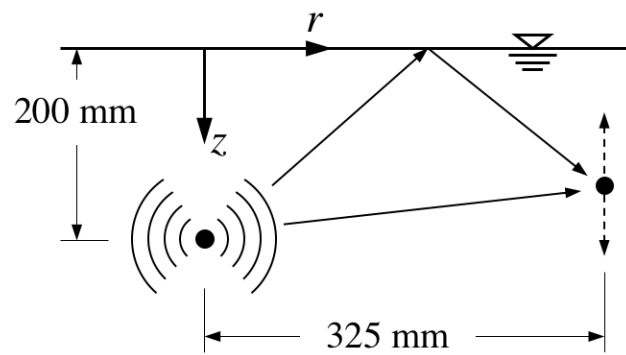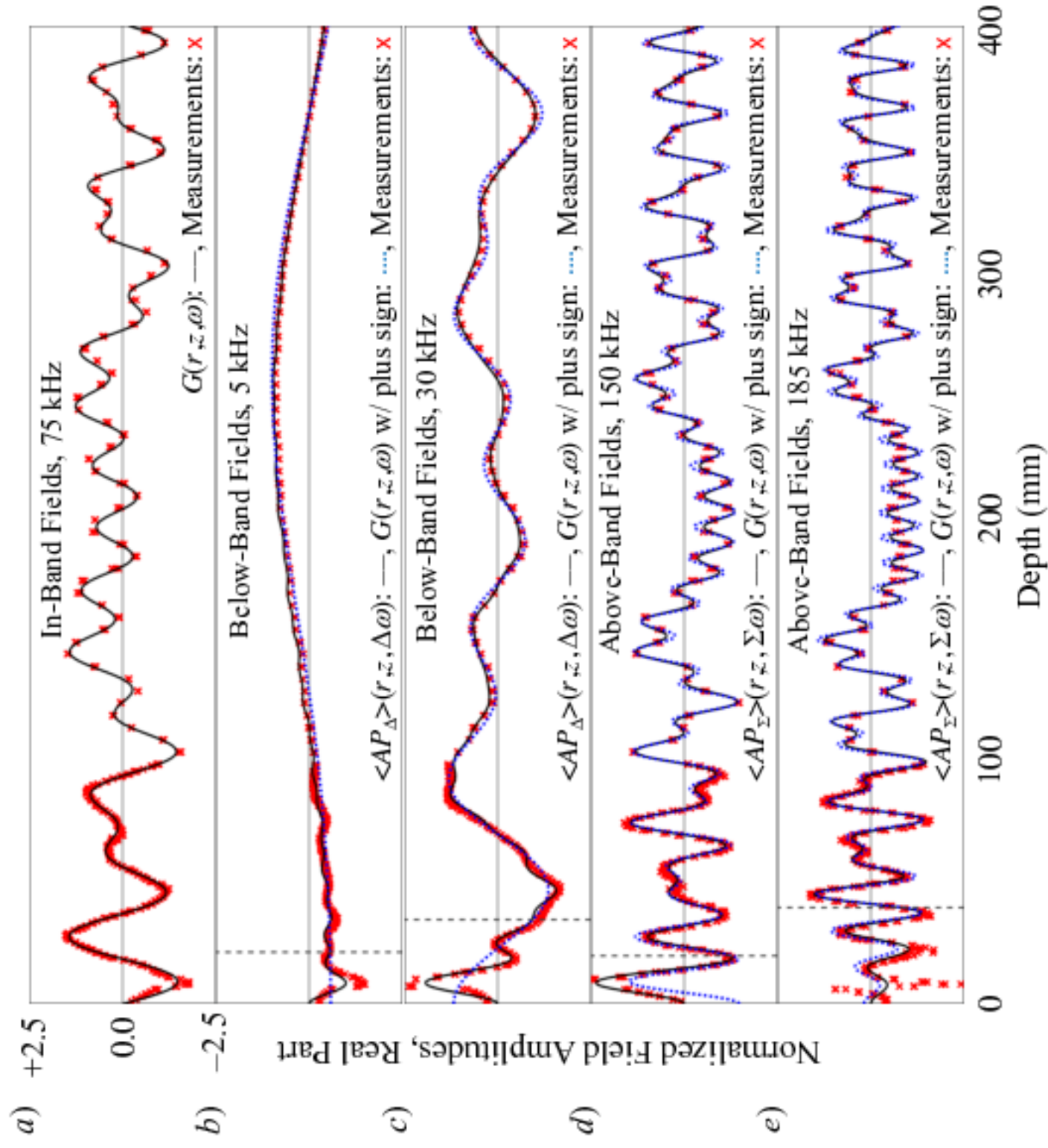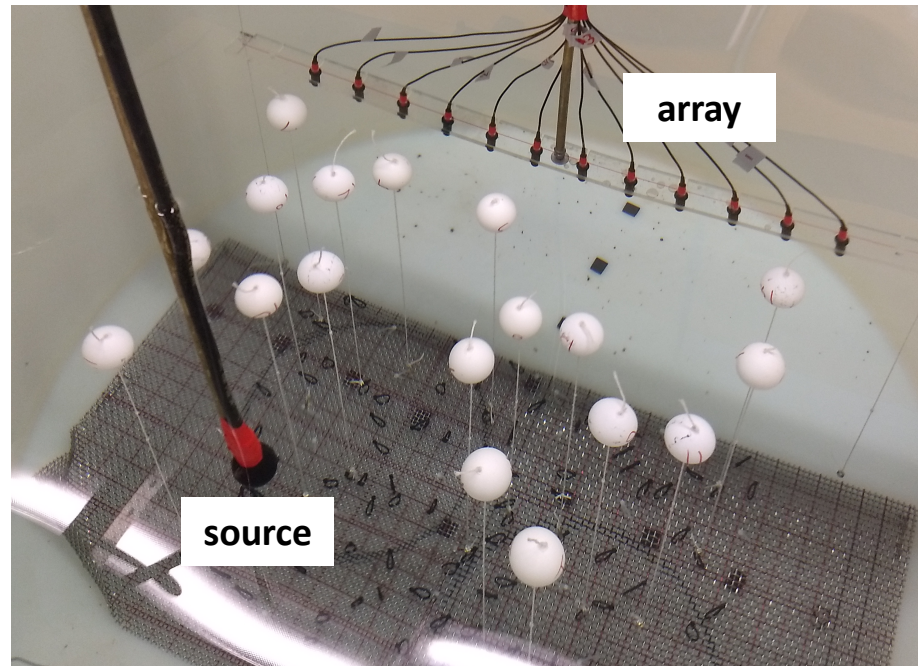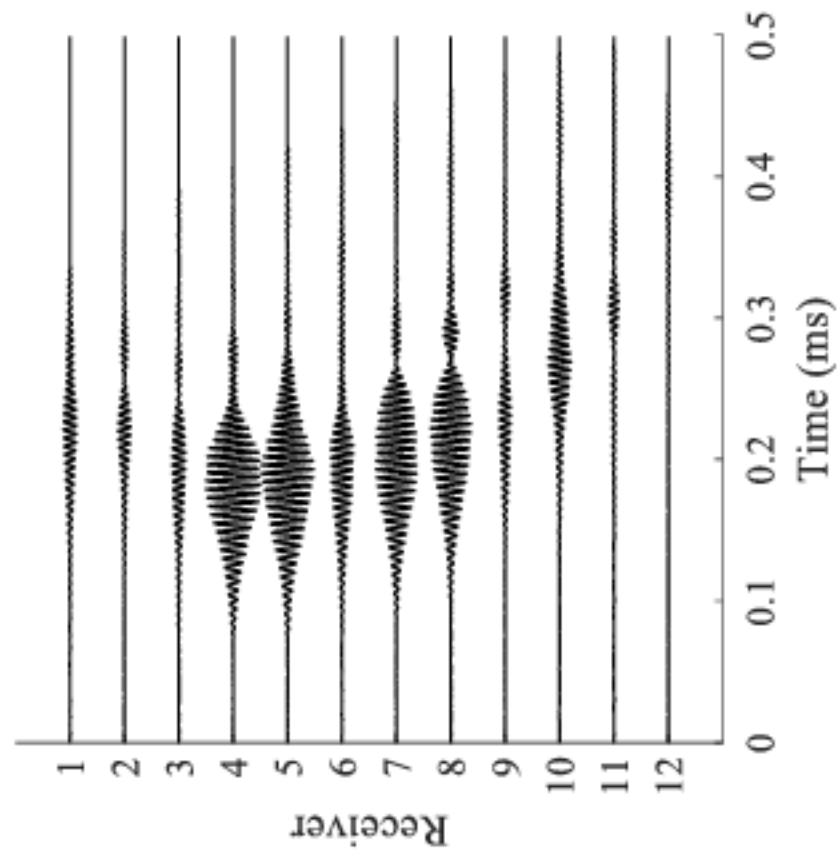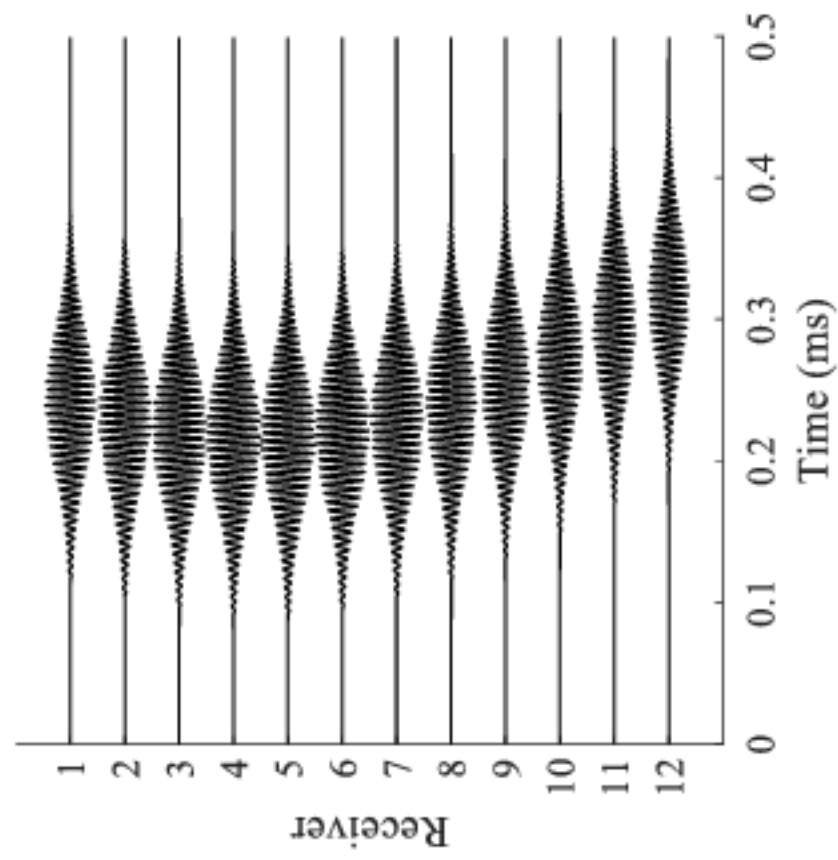
Fig. 1

Fig. 2
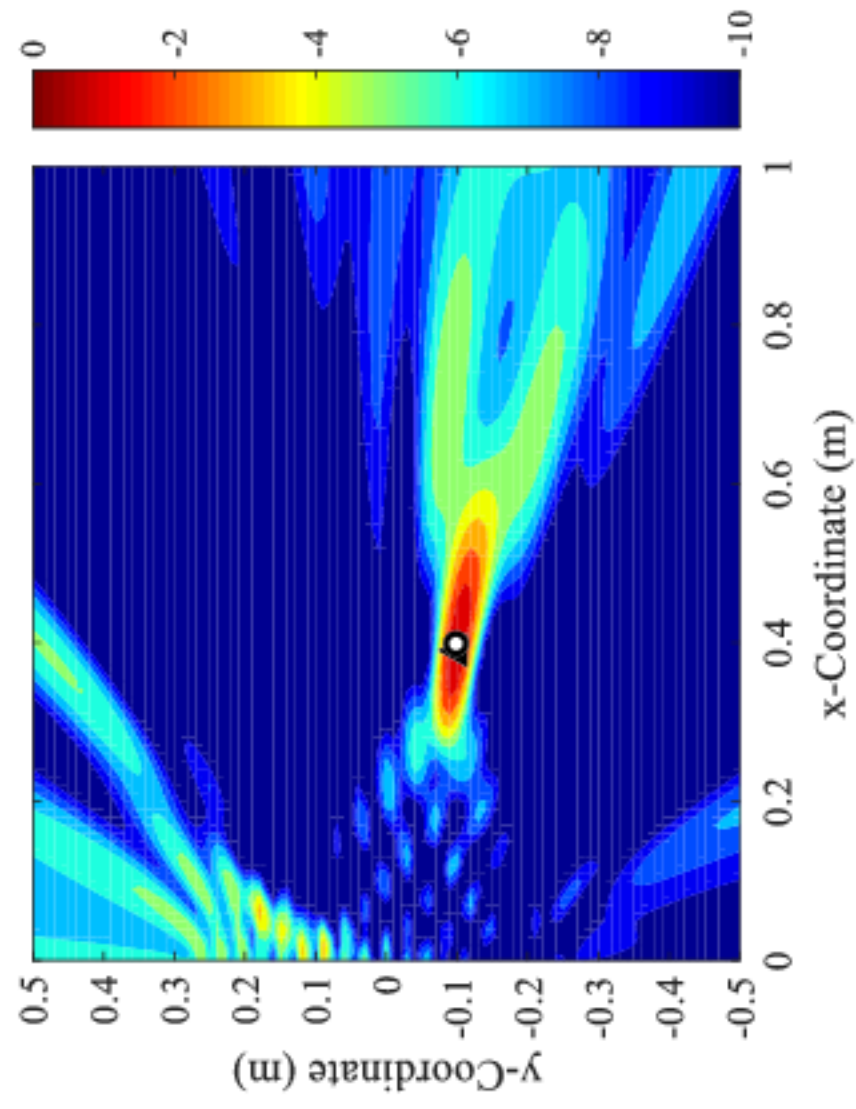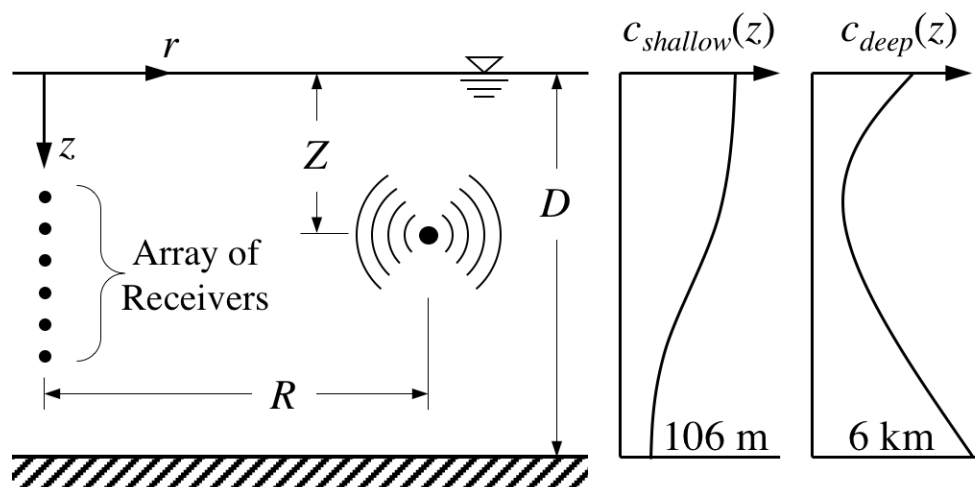
Fig. 3

Fig. 4

Fig. 5a)

Fig. 5b)

Fig. 6a)

Fig. 6b)

Fig. 7

Fig. 8a)

Impulse Response, Depth

41.2m

97.4m

Time Delays (ms)

Fig. 8b)

Impulse Response, Depth

41.2m

97.4m

Time Delays (ms)

0.0   2.5   5.0   7.5   10.0   12.5   15.0
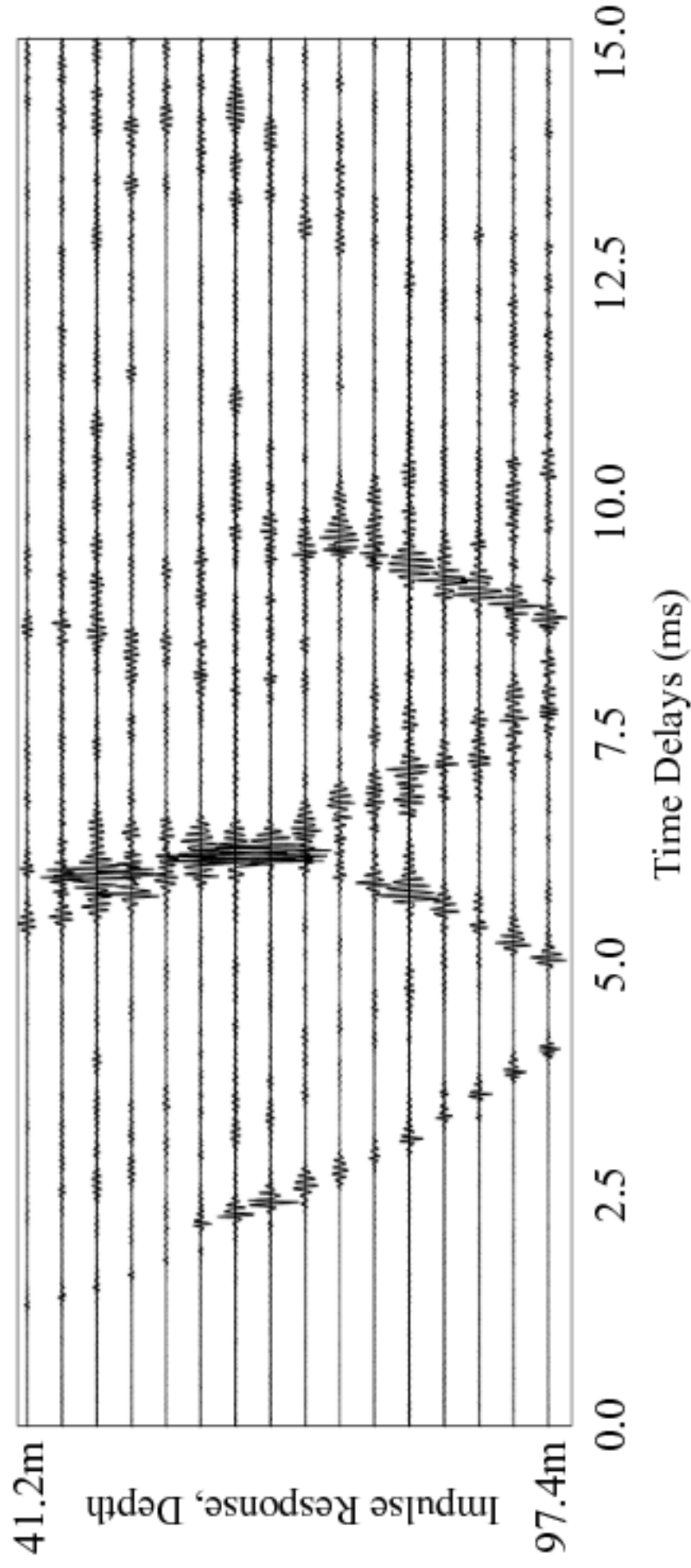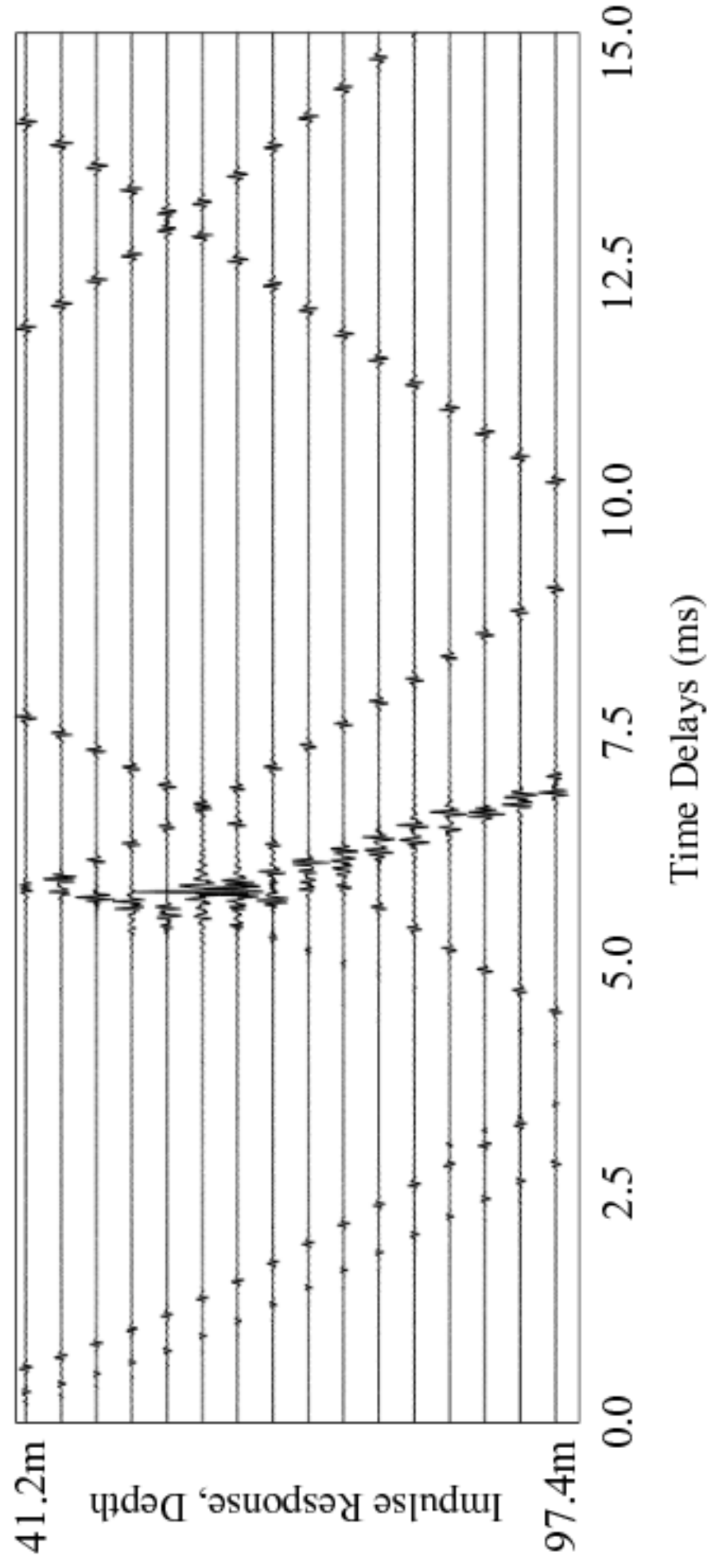
Fig. 9a)

Fig. 9b)

Fig. 10a)

Time After Transmission (s)

Depth (km)

Fig. 10b)

Time After Transmission (s)

Depth (km)

Fig. 11a)

Fig. 11b)